Buoyancy frequency profiles and internal semidiurnal tide turning depths in the oceans

Benjamin King,[1] Mark Stone,[1] H. P. Zhang,[1,2] Theo Gerkema,[3] M. Marder,[1] Robert B. Scott,[4,5] and Harry L. Swinney[1]

Received 13 October 2011; revised 31 January 2012; accepted 7 February 2012; published 4 April 2012.

[1] We examine the possible existence of internal gravity wave "turning depths," depths below which the local buoyancy frequency $N(z)$ becomes smaller than the wave frequency. At a turning depth, incident gravity waves reflect rather than reaching the ocean bottom as is generally assumed. Here we consider internal gravity waves at the lunar semidiurnal (M_2) tidal frequency, ω_{M2}. Profiles of $N^2(z)$ (the quantity in the equations of motion) are computed using conductivity, temperature, and depth data obtained in the World Ocean Circulation Experiment (WOCE). Values for $N^2(z)$ computed using Gibbs SeaWater routines in two thermodynamically equivalent expressions for $N^2(z)$ are found to yield values that are in excellent accord but differ significantly from $N^2(z)$ computed from often-used but inexact expressions that involve potential density. Uncertainties in $N^2(z)$ are estimated using a Monte Carlo method, where the data are averaged over a range in depth (80–200 m), which is determined by minimizing a cost function. Our principal result, reached from an analysis of all 18,000 WOCE casts, is that turning depths are common for zonal (east-west propagating) internal tides in the deep oceans. Inclusion of the full Coriolis effect (i.e., not making the so-called Traditional Approximation) leads to the conclusion that turning depths cannot occur for meridional and near-meridional internal tides, but the 'non-traditional' component has little impact on turning depths for internal tides that are near-zonal (i.e., propagating within about 30° of the east-west direction) at low and midlatitudes.

Citation: King, B., M. Stone, H. P. Zhang, T. Gerkema, M. Marder, R. B. Scott, and H. L. Swinney (2012), Buoyancy frequency profiles and internal semidiurnal tide turning depths in the oceans, *J. Geophys. Res.*, *117*, C04008, doi:10.1029/2011JC007681.

1. Introduction

[2] Internal gravity waves reflecting from bottom topography represent an important phenomenon in ocean dynamics. We are concerned here particularly with M_2 internal tides, i.e., internal waves at the semidiurnal lunar frequency, 1.4052×10^{-4} rad/s. These internal tides represent an important class of internal waves in the ocean, dominating the energy spectrum along with near-inertial internal waves.

[3] The reflection of internal tides from topography can locally render the stratification unstable [*Gemmrich and van Haren*, 2001]; more generally, they are thought to play a significant role in ocean mixing [*Garrett and St. Laurent*, 2002]. Reflection is accompanied by strong intensification when the bottom slope is critical [*Eriksen*, 1982; *Zhang et al.*, 2008], i.e., when the direction of wave-energy is along slope; overturning may then occur, resulting in mixing.

[4] All this presumes that internal waves can reach the bottom in the first place. However, *Munk* [1981] suggested the possibility of *turning depths*, depths at which a transition would occur from $N(z) > \omega$ to $N(z) < \omega$, where N is the buoyancy frequency and ω the wave frequency. Below the turning depth, wave propagation would not be possible. This can be seen from the expression for the steepness μ of wave-energy propagation, where $\mu = \tan\psi$ (with ψ the angle of the wave-energy propagation direction with respect to the horizontal)

$$\mu = \pm\left(\frac{\omega^2 - f^2}{N^2 - \omega^2}\right)^{1/2}, \tag{1}$$

where f is the Coriolis parameter, $f = 2\Omega\sin\phi$ (with Ω the Earth's angular velocity and ϕ the latitude). Assuming that $|f| < \omega$, we see that the expression in parentheses turns negative when $N < \omega$, indicating that waves cease to propagate. At such a turning depth, internal waves reflect. Thus,

[1]Center for Nonlinear Dynamics and Department of Physics, University of Texas at Austin, Austin, Texas, USA.
[2]Now at Institute of Natural Sciences and Department of Physics, Shanghai Jiao Tong University, Shanghai, China.
[3]Royal Netherlands Institute for Sea Research, Texel, Netherlands.
[4]Département de Physique et Laboratoire de Physique des Océans, Université de Bretagne Occidentale, Brest, France.
[5]Institute for Geophysics, University of Texas at Austin, Austin, Texas, USA.

0148-0227/12/2011JC007681

internal waves would not reach the bottom if the deep layers were so weakly stratified that $N(z) < \omega$.

[5] Internal wave reflection at a turning depth has been examined theoretically by *Kistovich and Chashechkin* [1988], and recent experiments have examined internal wave propagation in nonuniform density stratifications [*Mathur and Peacock*, 2009, 2010; *Gregory and Sutherland*, 2010]. However, oceanic data have not been previously examined to determine whether turning depths actually occur for internal M_2 tides. In this paper, we examine the WOCE CTD data (current and temperature data as a function of depth) to address the question: *Are there locations in the oceans where there exist robust turning depths below which* $N(z) < \omega_{M2}$?

[6] Before searching for the existence of turning depths, we must address three fundamental issues. The first concerns the correct definition of N. This can be found in textbooks, but misconceptions still abound. Some widely used scripts unnecessarily adopt an inexact expression, the error from which becomes significant in the weakly stratified abyssal ocean.

[7] The second issue concerns the noisy nature of buoyancy frequency profiles $N(z)$ deduced from CTD data. The wiggles in these vertical profiles can largely be ascribed to inaccuracies in salinity values. We will describe a procedure for obtaining buoyancy frequency profiles with sufficiently small statistical uncertainty to make it possible to address the turning depth question. First, a buoyancy frequency profile is calculated for temperature and salinity measurements that have been averaged over some arbitrarily selected depth, typically 100 m, to reduce the noise. Then a Monte Carlo method is used to determine confidence limits for the result. Finally, the optimum depth range for the averaging is determined by finding the minimum of a cost function. The full procedure yields $N(z)$ values in the deep ocean where we obtain a standard deviation of the mean significantly smaller than ω_{M2}.

[8] A third issue, deferred to the end of this paper, concerns the limited validity of equation (1) [*LeBlond and Mysak*, 1978; *Cushman-Roisin*, 1996; *Gerkema et al.*, 2008]. This expression is based on the so-called Traditional Approximation, in which the component of the Coriolis force proportional to the cosine of latitude is neglected. The approximation becomes invalid in weakly stratified layers where N is of the order of 2Ω, and equation (1) needs to be modified accordingly. Non-traditional effects create a horizontal anisotropy: internal waves propagating in the meridional direction behave differently from those propagating in the zonal direction. The consequences for the occurrence of turning depths will be discussed.

[9] The remainder of this paper is organized as follows. In section 2, we examine definitions of buoyancy frequency and the origin of the wiggles in buoyancy frequency vertical profiles calculated from CTD data. A method for smoothing these profiles is presented in section 3. In section 4, the WOCE CTD data base is searched for internal tide turning depths, which are found to occur at many locations in the deep ocean. Results are presented in particular for three WOCE ship transects, and a world map is presented showing the locations of all turning depths determined from the WOCE data. In addition, close-up maps are shown for three regions that have many locations with turning depths. The last part of section 4 examines turning depths for internal tides when the full Coriolis force is included in the momentum equations. Some consequences of this work are discussed in section 5.

2. Computation of $N^2(z)$

2.1. Exact Thermodynamic Expressions

[10] We consider $N^2(z)$ rather than $N(z)$ because N^2 is the quantity that appears in the equations governing the dynamics of internal waves; further, N^2 can become negative, which is not a problem unless one wants to calculate its square root, N.

[11] Gravitational stability of a stratified layer of seawater will here be considered with respect to *small vertical adiabatic* movements of water parcels. The smallness (strictly speaking infinitesimal) motions means that we are looking at *local* stability. The assumption that movements are adiabatic means that they must be fast enough to avoid an exchange of heat and salinity with the parcel's surroundings. With these assumptions one arrives at two equivalent expressions for N^2 [*Kamenkovich*, 1977; *Gill*, 1982; *Apel*, 1987]. One is in terms of the vertical gradient of *in-situ* density ρ

$$N^2 = g^2\left(\frac{d\rho}{dp} - \frac{1}{c_s^2}\right), \tag{2}$$

where g is the acceleration due to gravity, p is pressure, and c_s the adiabatic speed of sound.

[12] The other expression is in terms of vertical gradients of temperature T and Absolute Salinity S_A

$$N^2 = \rho g^2\left(\alpha\left[\frac{\alpha T}{\rho c_p} - \frac{dT}{dp}\right] + \beta\frac{dS_A}{dp}\right), \tag{3}$$

where α is the thermal expansion coefficient, β is the haline contraction coefficient, and c_p is the constant pressure specific heat. Derivatives are evaluated at the same pressure level n as their coefficients by using the centered scheme $(T_{n+1} - T_{n-1})/2\Delta p$ for dT/dp, and similarly for salinity and density.

[13] While equations (2) and (3) are theoretically equivalent, differences will occur if the various state variables are evaluated by equations of state that are inconsistent, which happens when, for example, the equations of state for ρ and c_s are based on different sets of measurements. This problem can be avoided if one uses the 'master' equation of state for the Gibbs potential, from which all the other state variables follow; then they are consistent by construction [*Feistel and Hagen*, 1995; *Feistel et al.*, 2008]. As a result, it is immaterial which of the two equations, (2) or (3), is being used; in our calculations we find that the outcomes differ by a mere 0.1%.

[14] The most recent version of the Gibbs equation of state for seawater is TEOS-10 (http://www.teos-10.org) [*Intergovernmental Oceanographic Commission*, 2010], which we use here. Compared to earlier versions, the collection of Gibbs SeaWater routines now includes various quantities besides the standard state variables. The state variables in TEOS-10 are functions of pressure, temperature and *Absolute* Salinity S_A (g/kg). Absolute Salinity differs from the still more commonly used *Practical* Salinity S_P in

Table 1. Quantities in Equations (2) and (3) and the MATLAB Routines in TEOS-10 Used to Calculate Them[a]

Quantity	MATLAB Routine
absolute salinity S_A	gsw_SA_from_SP.m
in-situ density	gsw_rho.m
speed of sound c_s	sound_speed.m
thermal expansion α	gsw_alpha_wrt_t.m
haline contraction β	gsw_beta_const_t.m
specific heat c_p	gsw_cp.m
gravity g	gsw_grav.m
height from pressure	gsw_z_from_p.m

[a]All variables depend on pressure, temperature, and Absolute Salinity S_A, except the first, which has as input Practical Salinity S_P and geographical location, and the next to last, which has as input pressure and geographical location.

that S_A derives not merely from conductivity but also takes into account the small geographical differences in the constituents of salt.

[15] For clarity, we list in Table 1 the routines that we use in the application of equations (2) and (3). These routines are in terms of gradients with respect to pressure p rather than the vertical coordinate, because the former can be more easily calculated on the basis of WOCE CTD data, with its equidistant pressure levels Δp. However, in our figures we will present results as a function of depth rather than pressure, using the TEOS-10 'height from pressure' routine for the conversion.

2.2. Potential Density

[16] Even though two exact and easily usable expressions exist, (2) and (3), there is still an inexplicable temptation to adopt an incorrect definition of N^2 [e.g., see *Wunsch and Ferrari*, 2004]. A widely used script (sw_bfrq.m) is based on an incorrect definition of N^2, as in, e.g., CSIRO SeaWater library, recently superseded by Gibbs SeaWater (TEOS-10),

$$-\frac{g}{\rho_{pot}}\frac{d\rho_{pot}}{dz}, \tag{4}$$

where ρ_{pot} is potential density. It was already pointed out by *Lynn and Reid* [1968] that the gradient of potential density underestimates the strength of the stability, especially in the deep western Atlantic Ocean, even to the point where it suggests instability when, in fact, the water column is stable, as is borne out by the exact definitions (2) and (3). Using the N^2 expression based on potential density, we find in our analysis of the WOCE data nearly twice as many locations with turning depths as we find when we use the exact definitions for N^2. This stands as a reminder of previous warnings [e.g., *Lynn and Reid*, 1968; *Gill*, 1982] against the use of the potential density expression.

2.3. Application to WOCE Data

[17] Returning to the correct expressions, (2) and (3), we can anticipate the wiggly nature of N^2 when calculated from CTD data and identify the main cause of these wiggles. WOCE guidelines for CTD measurements state that for temperature the required accuracy is 2 mK and precision is 0.5 mK; for salinity the required accuracy is 2 mS [0.002S] and precision is 1 mS [*Joyce*, 1988; *Joyce and Corry*, 1994]. The stated precisions for WOCE temperature (0.5 mK) and salinity (1 mS) measurements imply that the latter contributes about ten times more strongly to wiggles in N^2, for its coefficient β magnifies the noise in measurements of S by a factor of four to five times more than does α with noise in T. Note that in discussing the WOCE data we follow the WOCE nomenclature and use S for salinity; this is *Practical* Salinity S_P, not *Absolute* Salinity S_A. The TEOS-10 routine that we use to convert Practical Salinity to Absolute Salinity is listed in Table 1.

[18] To illustrate the wiggly nature of N^2 calculated from CTD data, we consider an imaginary case in which the real salinity is vertically uniform, so that the last term in (3) should be zero. However, the stated precision means that the measured salinity may differ from one pressure level to the next by ± 2 mS. With steps in pressure of 2 dbars, this results in values of N^2 (due to the salinity term alone) of order $\pm 10^{-5}$ rad^2/s^2, which is of the same order as the mean value of N^2 in the ocean (and three orders of magnitude

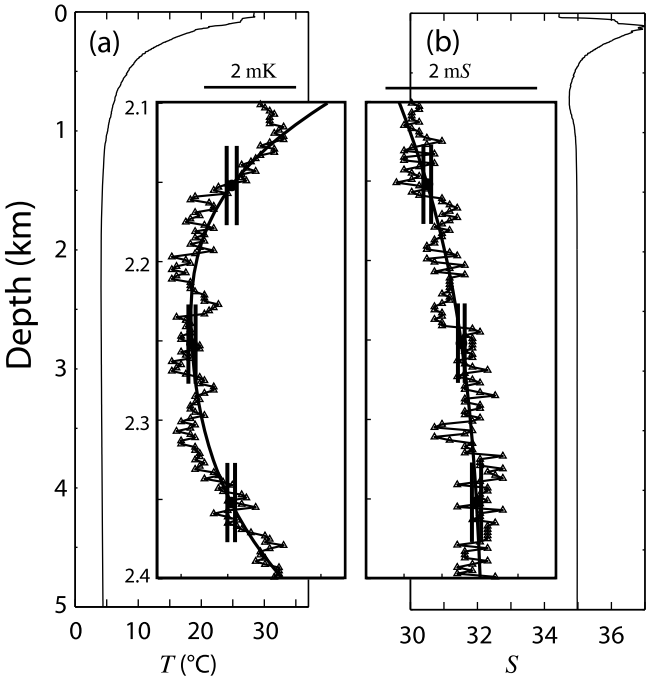

Figure 1. Profiles for (a) temperature $T(z)$ and (b) Practical Salinity $S(z)$ from a WOCE CTD cast appear smooth when plotted over the full depth range, but on the expanded scale of the insets the data (triangles) at 2 m intervals look noisy. This noise leads to large fluctuations in the buoyancy frequency $N(z)$ computed by numerical differentiation, unless the T and S data are first averaged over depth. The large black dots in the insets are the average values of T and S in bins of depth 100 m. The standard deviation of the mean for each point (indicated by the vertical bars on each side of a black dot), computed by a Monte Carlo technique, are small compared to the stated accuracies of the WOCE temperature and salinity data, which are indicated by the horizontal bars above the insets. The smooth curves in the insets are cubic spline fits to the smoothed data. These WOCE data were obtained in the Venezuelan Basin in the Caribbean: cast A22-316N151-4-10, latitude 13.17°N, longitude 66.00°W.

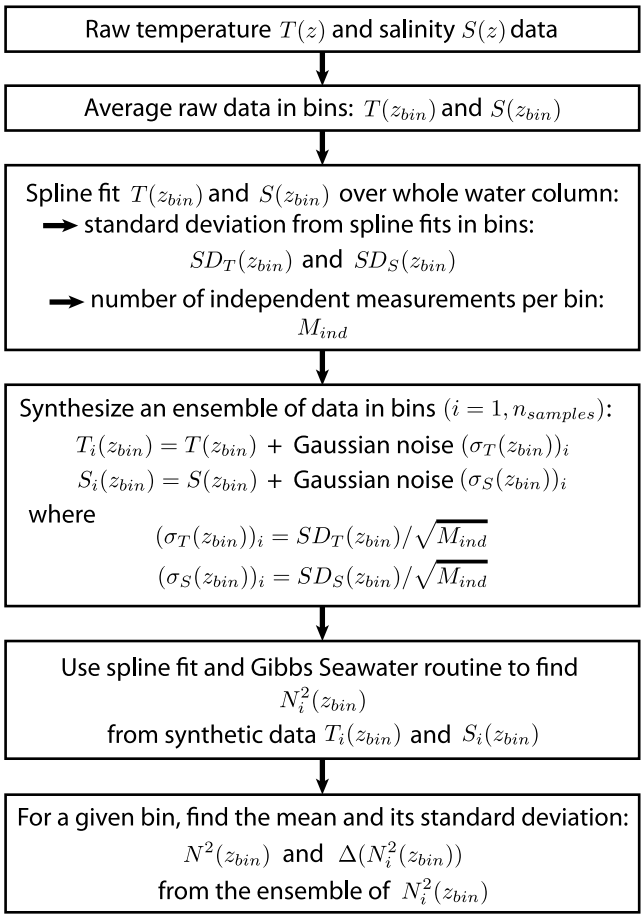

Figure 2. A flowchart for computing $N^2(z)$ and $\Delta(N^2(z))$ from a Monte Carlo analysis.

larger than ω_{M2}^2!). In other words, these wiggles are a dominant feature in the signal of N^2, even though, paradoxically, they stem from insignificant fluctuations in S. In section 3 we propose a method to remove them in a rational way.

2.4. WOCE Database

[19] The World Ocean Circulation Experiment [*National Oceanographic Data Center*, 2010] was conducted as a component of the World Climate Research Programme between 1990 and 1998; in addition, data from as early as 1985 have been incorporated into the database. The goal was to obtain a snapshot of the state of the ocean within a single decade. *In situ* measurements included CTD (conductivity, temperature, depth), sea level, and current (determined with current meters and Acoustic Doppler Current Profilers). Our analysis has been performed on the WOCE CTD survey obtained in about 120 zonal and meridional coast-to-coast transects (cruises across the world oceans), where a research vessel would stop and make measurements at regular intervals, typically 55 km [*World Ocean Circulation Experiment*, 1994].

3. Methods

[20] Profiles of temperature $T(z)$ and salinity $S(z)$ from a WOCE cast in the Venezuelan Basin are shown in Figure 1. The temperature and salinity appear to vary smoothly over the full 5 km deep water column, but the insets show that both quantities oscillate rapidly on small length scales. The magnitude of these oscillations is less than the precision given in the WOCE guidelines (see section 2.3). When the profiles are differentiated numerically to compute $N^2(z)$ from closely spaced measurements in a cast, fluctuations in T and S that are smaller than the precision of those measurements lead to large fluctuations in $N^2(z)$. Hence it is clear that some averaging of $T(z)$ and $S(z)$ over a range of depths is needed to reduce the noise. In the deep ocean $T(z)$ and $S(z)$ vary slowly with depth; hence, as we shall show, averaging the data over depths of 80–200 m can be justified.

3.1. $\Delta(N^2)$, the Experimental Standard Deviation of the Mean of $N^2(z)$

[21] To determine if there are indeed locations where $N^2(z) < \omega_{M2}^2$, an estimate is needed for the experimental standard deviation of the mean averaged over some depth [*Joint Committee for Guides in Meteorology*, 2008]. To do this we use a Monte Carlo method [*Joint Committee for Guides in Meteorology*, 2008; *Lemieux*, 2009], which is outlined in the flowchart in Figure 2.

[22] The first step of the data analysis is to divide the water column into bins of width Δ with data in a bin sampled at depth intervals δ; thus there are $n = \Delta/\delta$ points in a bin. The $T(z)$ and $S(z)$ data in each bin are averaged to obtain $T(z_{\mathrm{bin}})$ and $S(z_{\mathrm{bin}})$, where z_{bin} is the center of the bin. The depth range of the bins in which the $T(z)$ and $S(z)$ data can be averaged to reduce noise without overly smoothing the data is not known *a priori*, so we begin by arbitrarily choosing a depth of 100 m for averaging. In section 3.2 the optimum depth range for averaging a given set of data is determined by minimizing a cost function.

[23] $N^2(z)$ is computed using the results from spline fits to $T(z_{\mathrm{bin}})$ and $T(z_{\mathrm{bin}})$ in the Gibbs SeaWater routines in Table 1. The comparison between the results obtained for $N^2(z)$ from equations (2) and (3) proved to be a good self-consistency test.

[24] In the Monte Carlo analysis, $\Delta(N^2)(z_{\mathrm{bin}})$ depends on the number of effective degrees of freedom n_{nid} for the n values of temperature $T(z)$ and salinity $S(z)$ in a bin. The result from section *A1* gives $n_{\mathrm{nid}} = n\delta/(2\xi)$, where ξ is the correlation length. The correlation length was obtained by examining autocorrelation functions of the deviations of $T(z)$ and $S(z)$ from their means for many data sets (at depths greater than 4 km) at different locations. The autocorrelation functions for $S(z)$ typically decay by a factor of e over a depth of 2 m, and autocorrelation functions for $T(z)$ typically decay by a factor of e over a depth of 4 m. We conservatively assume that both T and S data are characterized by a 4 m vertical correlation length. Then we have

$$n_{\mathrm{ind}} = n\delta/2\xi = 50 \times (2\ \mathrm{m})/(2 \times (4\ \mathrm{m})) = 12.5. \qquad (5)$$

Then the experimental standard deviations of the mean, $\sigma_S(z_{\mathrm{bin}})$ and $\sigma_T(z_{\mathrm{bin}})$, are given by the root mean square difference between the raw data and the cubic spline within each bin, divided by the square root of n_{ind} (cf. Figure 2), i.e., $\sigma_S(z_{\mathrm{bin}}) = SD_S(z_{\mathrm{bin}})/\sqrt{n_{\mathrm{ind}}}$ and $\sigma_T(z_{\mathrm{bin}}) = SD_T(z_{\mathrm{bin}})/\sqrt{n_{\mathrm{ind}}}$.

[25] In the Monte Carlo method [*Joint Committee for Guides in Meteorology*, 2008] data sets are generated by

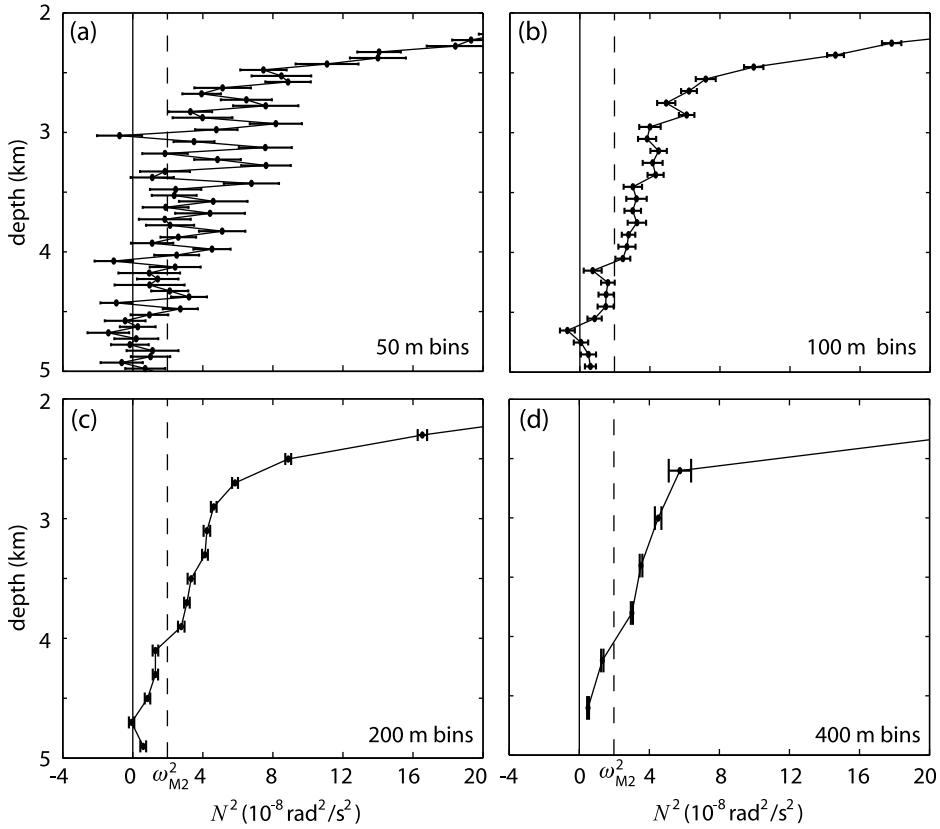

Figure 3. The effect of varying the bin width used for averaging the $T(z)$ and $S(z)$ data is illustrated by these profiles for $N^2(z)$ computed for the data set used in Figure 1. The experimental standard deviation of the mean for each point (indicated by bars on each side of the point) were calculated by the Monte Carlo method described in section 3.1. For all four bin widths it is evident that there is a turning depth at about 4.0 km.

adding to each value $S(z_{\text{bin}})$ and $T(z_{\text{bin}})$ random numbers chosen from Gaussian distributions with half-width $\sigma_S(z_{\text{bin}})$ and $\sigma_T(z_{\text{bin}})$. This ensemble of synthetic data is denoted as $S_i(z_{\text{bin}})$ and $T_i(z_{\text{bin}})$, where i represents different members of the ensemble with $n_{samples}$ samples ($i = 1, n_{samples}$). For each choice of random numbers, new spline fits were made and used in the Gibbs SeaWater routines to find $N^2(z_{\text{bin}})$ values. We varied $n_{samples}$ from 50 to 5000 and found that the results with 500 were close to that for 5000; subsequent analyses were done with $n_{samples} = 500$. For each depth z_{bin}, we found for each choice of bin size the mean, $N^2(z_{\text{bin}})$, and the experimental standard deviation of the mean, $\Delta(N^2)(z_{\text{bin}})$.

[26] The results for $N^2(z_{\text{bin}})$ for the data in Figure 1 are plotted with the experimental standard deviation of the mean $\Delta(N^2)(z_{\text{bin}})$ in Figure 3 for bin widths of 50, 100, 200, and 400 m. First consider bin width 100 m (Figure 3b), where $\Delta(N^2)(z_{\text{bin}})$ is typically $(0.3)\omega^2_{M2}$, small enough so that the data within a single bin can provide clear evidence of a turning depth. But there is not just a single bin with $N^2(z) < \omega^2_{M2}$, there are 9 consecutive such bins. This provides extremely strong evidence of the existence of a turning depth for these WOCE data. Our analysis of all the WOCE data reveals that $N^2(z)$ profiles from many CTD casts have a series of consecutive bins with $N^2(z) < \omega^2_{M2}$, which clearly indicates the existence of turning depths.

[27] For a bin width of 50 m, $N^2(z) < \omega^2_{M2}$ for the 10 deepest bins and for 22 of the 40 bins in the deepest 2000 m (Figure 3a). In the deepest 2000 m, a locally unstable profile is indicated by $N^2(z) < 0$ for 7 bins; however, none of the 7 bins is adjacent, and the experimental standard deviation of the mean for the individual points (indicated by the bars to either side of each point) are too large to conclude with confidence that the profile is indeed locally unstable.

[28] The 200 m and 400 m bins in Figures 3c and 3d provide very strong evidence for a turning depth. Note that the 400 m bin is so large that some z-dependence of N^2 is smoothed over.

3.2. Optimum Bin Size

[29] The optimum bin size for averaging data is computed in section *A2*. The result is that the optimum bin size Δ minimizes a cost function C, the Mean Integrated Square Error, which for $N^2(z)$ is

$$C = \left(\sum_m \left(N^2(z_{m+1}) - N^2(z_m) \right)^2 \right) \Delta, \qquad (6)$$

where z_m is the m-th bin in the vertical profile, and $\Delta = z_{m+1} - z_m$ is the size of a bin.

[30] Graphs of the cost function for $N^2(z)$ in the deep ocean are presented in Figure 4 for data obtained in casts on

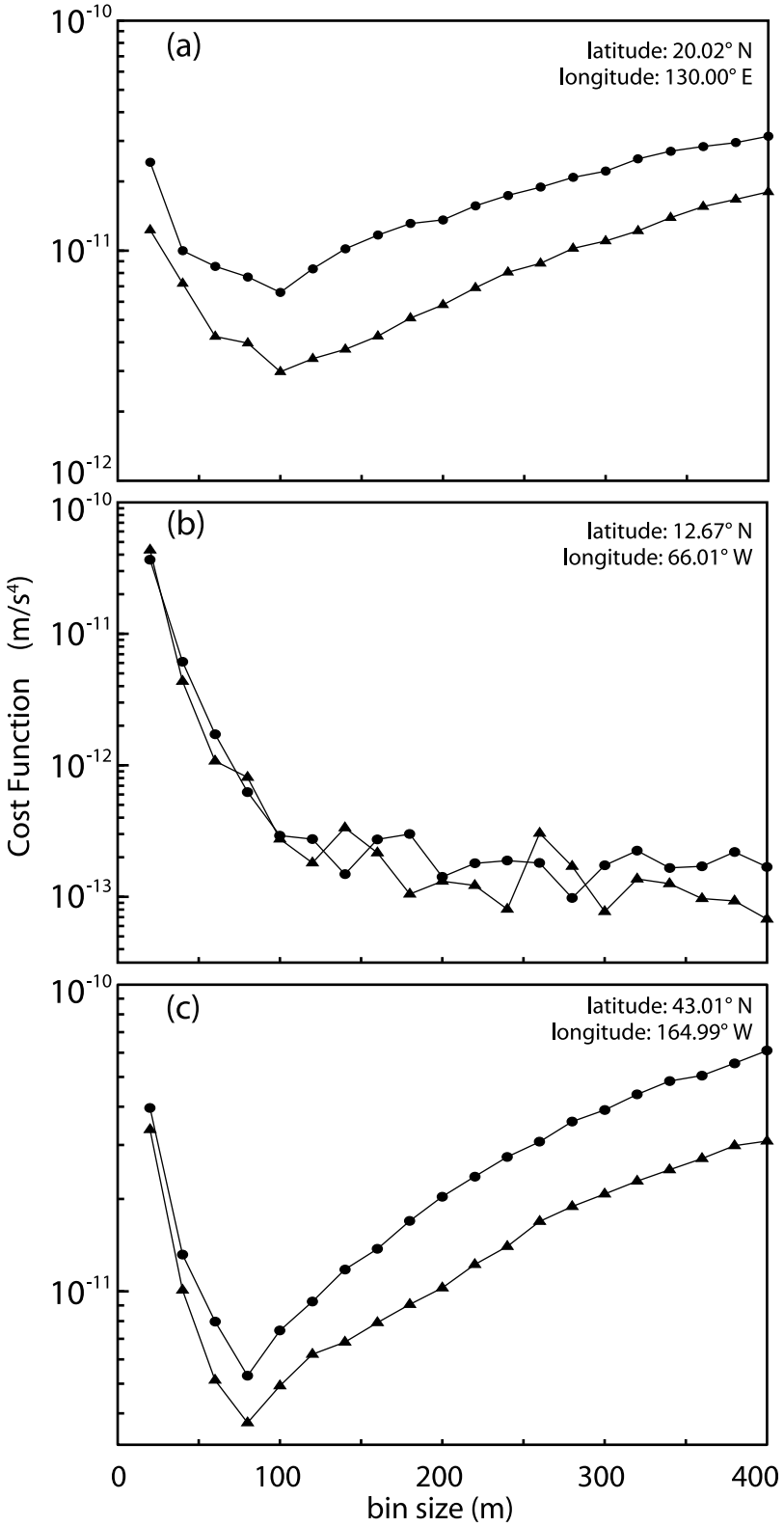

Figure 4. The optimum bin size for computing $N^2(z)$ is given by the minimum of a cost function, equation (6). An analysis of all WOCE data indicates the cost function minimum for data in the deep oceans occurs for bins typically 100 m in size, as illustrated here for data obtained below depths of 2500 m (circles) and 3000 m (triangles) from casts on WOCE transects (a) P08, (b) A22, and (c) P15, at the locations given. In Figure 4a the minimum is at about 100 m and in Figure 4c at 80 m; in Figure 4b the cost function rises sharply below bin widths of 100 m and is fairly flat (for the range shown) for bin sizes above 100 m.

three different transects; the routes of these transects are shown on the maps in the insets in Figure 6. The cost function graphs for data at depths greater than 2.5 km typically exhibit a minimum for bin sizes in the range 80–200 m. For example, the cost functions in Figures 4a and 4c have minima at 100 m and 80 m, respectively. Even when the cost function does not exhibit a clear minimum, as in Figure 4b, it rises rapidly for bin sizes below 100 m, indicating an optimum bin size of at least 100 m.

[31] We use for all subsequent analysis a bin depth of 100 m, which appears to strike a good balance between a bin sufficiently wide to reduce the noise through averaging and a bin narrow enough to preserve the structure in $N^2(z)$.

3.3. Generation of Transect Plots

[32] Results for $N^2(z)$ were computed for every cast in the WOCE data base. To determine the ocean depth at the location of a cast, we used *Smith and Sandwell*'s [1997] topography rather than the WOCE data because the 2 minute resolution in latitude and longitude of the Smith-Sandwell topography provides some indication of the roughness between the CTD stations, although the Smith-Sandwell underestimates the roughness for scales less than 10–20 km [*Goff*, 2010].

4. Results

4.1. Spatial and Temporal Variation of $N(z)$

[33] We compare results for buoyancy frequency profiles computed from measurements made at nearly the same location (within 0.03°) but by different ship transects at different times during the decade of the WOCE survey. For ease in interpretation, we present $N(z)$ profiles rather than the $N^2(z)$ discussed in section 3. (Since $N^2 > 0$ for the data presented in this section, we simply take the square root [*King*, 2010].)

[34] For depths greater than 1 km, the $N(z)$ profiles at each location exhibit very small variability over periods of months and even years, as can be seen in the nine groups of data presented in Figure 5. For example, note the small variations in the $N(z)$ profiles in data group 9 (for a 3 month period), group 4 (5 years), and group 8 (6 years). The variability is larger in some cases, as illustrated by the data in group 1 (2 days) and group 7 (same day).

[35] The results in data group 8 in Figure 5 provide a striking demonstration that 'yes' is the answer to the question that motivated our study: can $N(z)$ be determined from the WOCE data with sufficiently small uncertainty to determine whether there exist turning depths? No statistical analysis is needed to see that the variation in $N(z)$ determined from data obtained by three ships over a six year period is small compared to ω_{M2}. Over such a long period $N(z)$ could change because of instrumental noise, instrument calibration, passing waves, plumes, currents, and mixing; hence the observed stationarity clearly demonstrates that data from a single WOCE cast can have a measurement uncertainty less than ω_{M2}.

[36] Another check on the buoyancy frequency results could be made if mooring data for internal tide wavelengths were available for the WOCE data sites. Then the internal tide wavelength could be independently computed by integrating the equation for the vertical velocity using buoyancy frequency values computed from the Gibbs routines.

4.2. Dissolved Oxygen

[37] The concentration of dissolved oxygen can be used as a rough indicator of age of a given water mass [*Kortzinger et al.*, 2004]. Water is oxygenated at the ocean surface, below which the dissolved oxygen is gradually removed. A lower concentration of dissolved oxygen suggests that the water has been below the surface for a longer period of time; however, it is nontrivial to use dissolved oxygen to establish a quantitative age.

[38] We examine the dissolved oxygen data from the World Ocean Atlas [*National Oceanographic Data Center*, 2005] to determine whether the water masses in bounded basins have properties different from nearby water at the same depth. The WOA2005 data tables give the observed dissolved oxygen level as a percentage of the saturation level at the local temperature and salinity values; the data are given on a 1 degree grid with 500 m vertical resolution.

[39] The dissolved oxygen measurements for the WOCE transects (shown as insets in Figure 6) reveal that water with turning depths in the enclosed basins in Figures 6b and 6c has oxygen content that is indeed significantly lower (more blue colored) than the water without turning depths at the same depth (more yellow than blue). However, in contrast, the region with turning depths in Figure 6a does not have confining topography, and the oxygen concentration in that region is not markedly different from outside that region.

4.3. Ubiquity of Turning Depths

[40] The world map in Figure 7 presents results obtained from analyses of all the Conductivity-Temperature-Depth data sets in the WOCE data base. The casts yielding turning depths are indicated as red dots, while casts with no turning depths are shown as blue dots. Only robust turning depths are shown, i.e., the red dots correspond to casts where the analysis yielded $N(z) < \omega_{M2}$ in at least two successive 100 m wide bins. Figure 7 shows that turning depths for the internal tides occur in many places in the oceans, including the Philippine Sea, the northern Pacific Ocean, the Pacific Ocean northeast of New Zealand, the central Indian Ocean, various regions in the Atlantic Ocean, and the Venezuelan Basin. Individual cast locations (shown as dots) are distinguishable in Figure 8, which shows three regions on a smaller scale than in Figure 7; many of the dots are red, indicating the presence of a robust turning depth.

[41] Table 2 summarizes the results for turning depths found in the WOCE data. The percentage of WOCE casts with turning depths for different depth ranges is given in the With Turning Depths column. Robust turning depths were found for 327 of the 6850 WOCE casts made at locations where the depth exceeded 4 km (54.3% of the oceans). Not surprisingly, most turning depths (250) occur where the depth exceeds 5 km. (Seafloor column gives the fraction of the seafloor in a given depth interval; this was calculated by numerically integrating over the *Smith and Sandwell* [1997] topography data with 2 minute resolution at 2 degree intervals in both latitude and longitude.)

4.4. Dependence of Turning Depths on Latitude and Beam Direction

[42] The Coriolis force has traditionally—and in previous sections—been approximated by including only the terms proportional to the sine of latitude, neglecting the ones

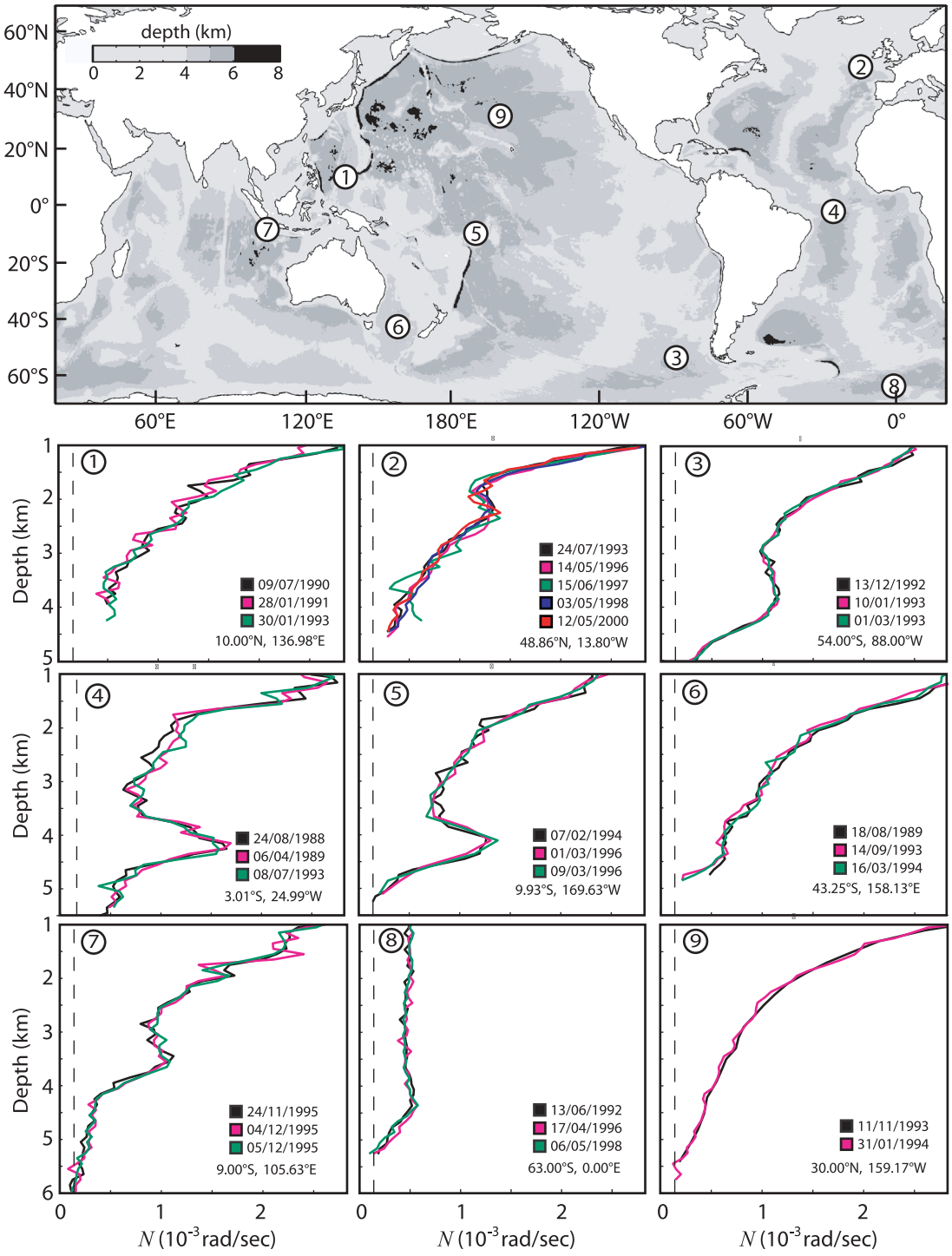

Figure 5. Buoyancy frequency profiles $N(z)$ for the nine locations given by circled numbers on the map. Each group of profiles was computed from WOCE data obtained within only 0.03° latitude and longitude. At each location there is little variation in $N(z)$ in independent measurements made over periods as long as six years. In contrast, there are dramatic differences in the $N(z)$ profiles for different locations. The vertical dashed line in each of the nine panels corresponds to ω_{M2}, the frequency of the M_2 tide. The map gray bar indicates ocean depth.

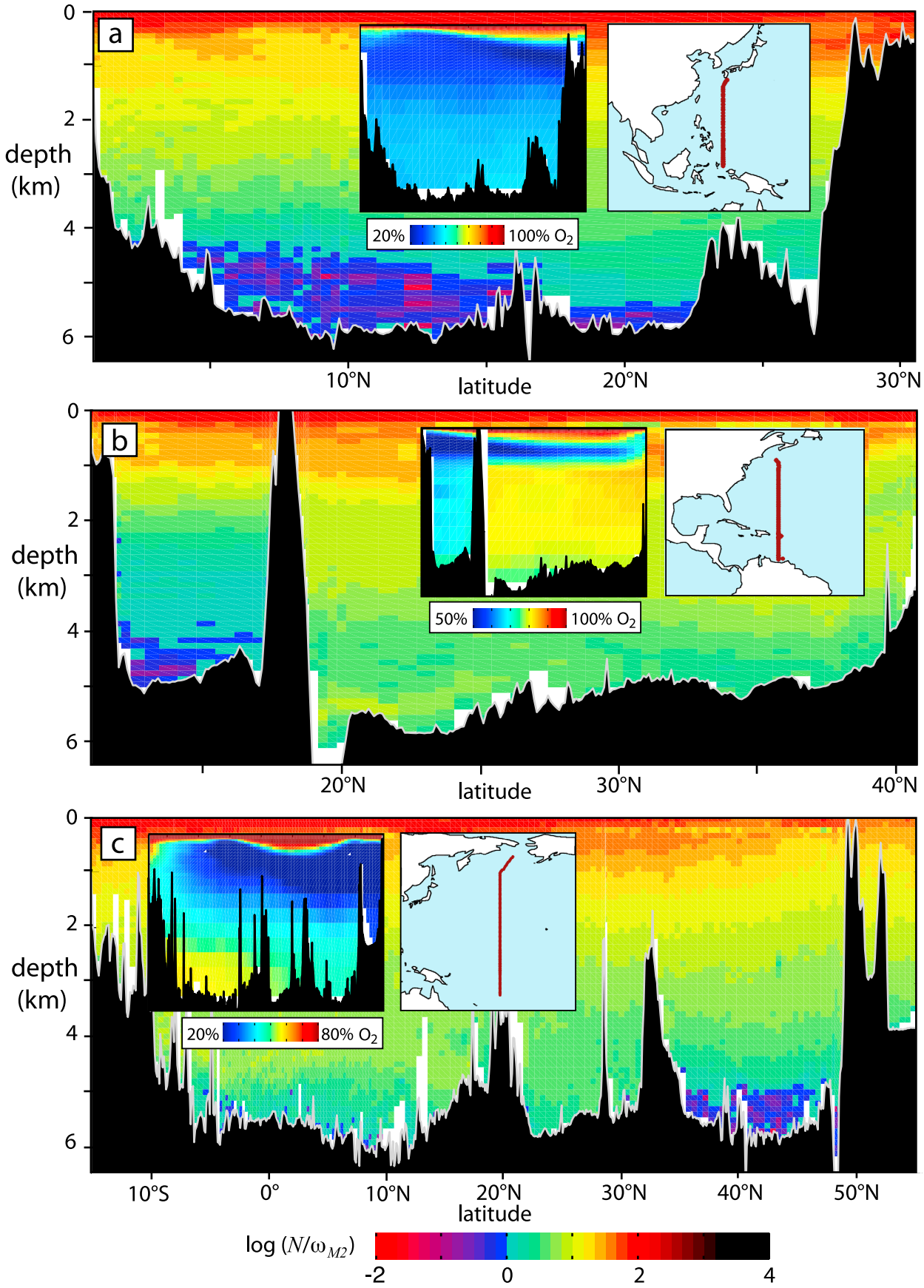
a
depth (km)
0
2
4
6
20% 100% O2
10°N
latitude
20°N
30°N
b
depth (km)
50% 100% O2
20°N
latitude
30°N
40°N
c
depth (km)
20% 80% O2
10°S
0°
10°N
20°N
latitude
30°N
40°N
50°N
log (N/ω M2)
-2
0
2
4

Figure 6

proportional to the cosine of latitude. While the former act purely in the horizontal plane, the latter involve also vertical movements (see *Gerkema et al.* [2008] for an overview). So, this is a good approximation for waves traveling at small angles with respect to the horizontal (i.e., low steepness), which is the case most often considered, but we are concerned here with internal waves approaching the vertical propagation direction as $N(z) \rightarrow \omega_{M2}$, so the cosine component of the Coriolis force can no longer be ignored. It breaks the symmetry in the horizontal plane and hence introduces a dependence on the direction of wave propagation in this plane; we denote by α the angle of propagation, north of east. The inclusion of the full Coriolis force modifies equation (1) to

$$\mu = \frac{B \pm (B^2 - AC)^{1/2}}{A}, \tag{7}$$

where $A = N^2 - \omega^2 + f_s^2$, $B = ff_s$, and $C = f^2 - \omega^2$; here $f_s = 2\Omega \cos\phi \sin\alpha$ is the 'non-traditional' Coriolis component [*Gerkema et al.*, 2008]. Among the several implications of (7), the most important one for our analysis is the fact that wave propagation can only occur if $B^2 - AC > 0$. Satisfying this criterion for wave frequency ω_{M2}, wave propagation angle α, and latitude ϕ may put restrictions on N. By setting $B^2 - AC = 0$, the critical value is readily obtained

$$N_{crit}^2 = \omega^2 \frac{f^2 + f_s^2 - \omega^2}{f^2 - \omega^2}. \tag{8}$$

For an internal tide propagating east-west (i.e., zonally, $\alpha = 0$), we have $f_s = 0$, and we are back to the traditional case, $N_{crit} = \omega_{M2}$.

[43] In contrast, for meridionally propagating internal tides ($\alpha = 90°$), the numerator in (8) becomes $4\Omega^2 - \omega_{M2}^2$, which is independent of latitude and always positive; since the denominator in (8) is negative on the equatorial side of the inertial latitude (74.5°N/S for M_2-internal tides), this means that N_{crit}^2 is negative, so there is no critical value for N in real terms. In other words, meridionally propagating internal M_2-tides can propagate in layers of any N and will not encounter a turning depth. This is a strong departure from the result that one finds under the Traditional Approximation.

[44] For lower angles, the situation is illustrated in Figure 9. Strong departures from the traditional case (dashed line) always occur as one approaches the inertial latitude, but closer to the equator, the departure from the traditional case becomes modest for internal tides that are nearly zonal ($\alpha < 30°$); the critical value of N at latitudes up to about 60° is then only a few percent smaller than for the zonal internal tides considered in previous sections.

5. Discussion

[45] Our analysis of WOCE conductivity-temperature-depth (CTD) data reveals that there are many locations in the world's deep oceans where there are turning depths, below which $N(z) < \omega_{M2}$ and zonal internal M_2 tides cannot propagate (see Figures 7 and 8). In some cases the turning depth is more than 1 km above the seafloor. A related study was conducted by *van Haren and Millot* [2006], who examined inertio-gravity wave propagation in the Algerian Basin of the Mediterranean Sea. They analyzed high resolution CTD data, obtained using a Sea-Bird 911*plus* probe, and found that neutral stability $N(z) = 0$ could be determined to $(0.8)f$ with averaging over 100 dbar, and to $0.4f$ with averaging over 600 dbar.

[46] Our analysis of WOCE data, averaged over depths of 100 m, yields an experimental standard deviation of the mean that is typically $(0.3)\ \omega_{M2}^2$, which is small enough to determine *from a single WOCE cast* whether there exists a turning depth for M_2 internal tides, as Figure 3 illustrates for a cast in the Venezuelan Basin. The experimental standard deviation of the mean can be reduced to nearly $(0.1)\ \omega_{M2}^2$ by averaging over a depth of 400 m, which is appropriate at depths below about 4 km, where N is small (e.g., see Figure 3).

[47] We have examined $N(z)$ profiles obtained on different ship transects during the WOCE decade, and we find the change in these profiles at a given location is in many cases very small over periods of years. In contrast, profiles at different locations are often quite different. For example, compare the results in Figure 5 for two locations in the western Pacific, data groups 1 and 5.

[48] Some $N(z)$ profiles exhibit an interesting peak at a depth of about 4 km, as can be seen in Figure 5 in group 3 at 3.7 km depth (Pacific Ocean, 54.0°S), group 4 at 4.2 km depth (Atlantic Ocean, 3.0°S), group 5 at 4.2 km depth (Pacific Ocean, 9.9°S), and group 7 at 3.6 km depth (Indian Ocean, 9.0°S). The existence of a similar peak in $N(z)$ at multiple locations, each observed in independent measurements made over a period of time by different instruments, indicates that the peak is neither a localized nor a transitory phenomenon. The presence of these peaks reflects a transition between water masses, with deep water of North-Atlantic origin lying over Antarctic Bottom Water, a transition that is also marked by strong vertical gradients in oxygen and silicate concentration [*van Aken*, 2006].

[49] Turning depths can insulate propagating internal wave beams from the seafloor, which in many regions is an efficient scatterer of internal waves. Understanding how turning depths might prevent internal tides from interacting with the seafloor will help pinpoint where internal waves deposit their energy, resulting in local mixing and a corresponding increase in the potential energy of the water column. Another effect that well-mixed regions (i.e., regions with small N) in the deep ocean could have is a reduction in internal wave energy radiated by rough topography that is fully or partially below a turning depth. Topographic features that would otherwise be very efficient scatterers of

Figure 6. Turning depths for zonally propagating internal waves at frequency ω_{M2} are evident in these transects as an abrupt change from light green (where $N(z) > \omega_{M2}$) to dark blue (where $N(z) < \omega_{M2}$) (cf. logarithmic color bar). These results were computed from WOCE transects (a) P08, (b) A22, and (c) P15, whose routes are shown by the red lines in the right-hand insets. The turning depths in Figures 6b and 6c are in water trapped in basins where the percentage of dissolved oxygen relative to saturation is low, as shown in the insets on the left.

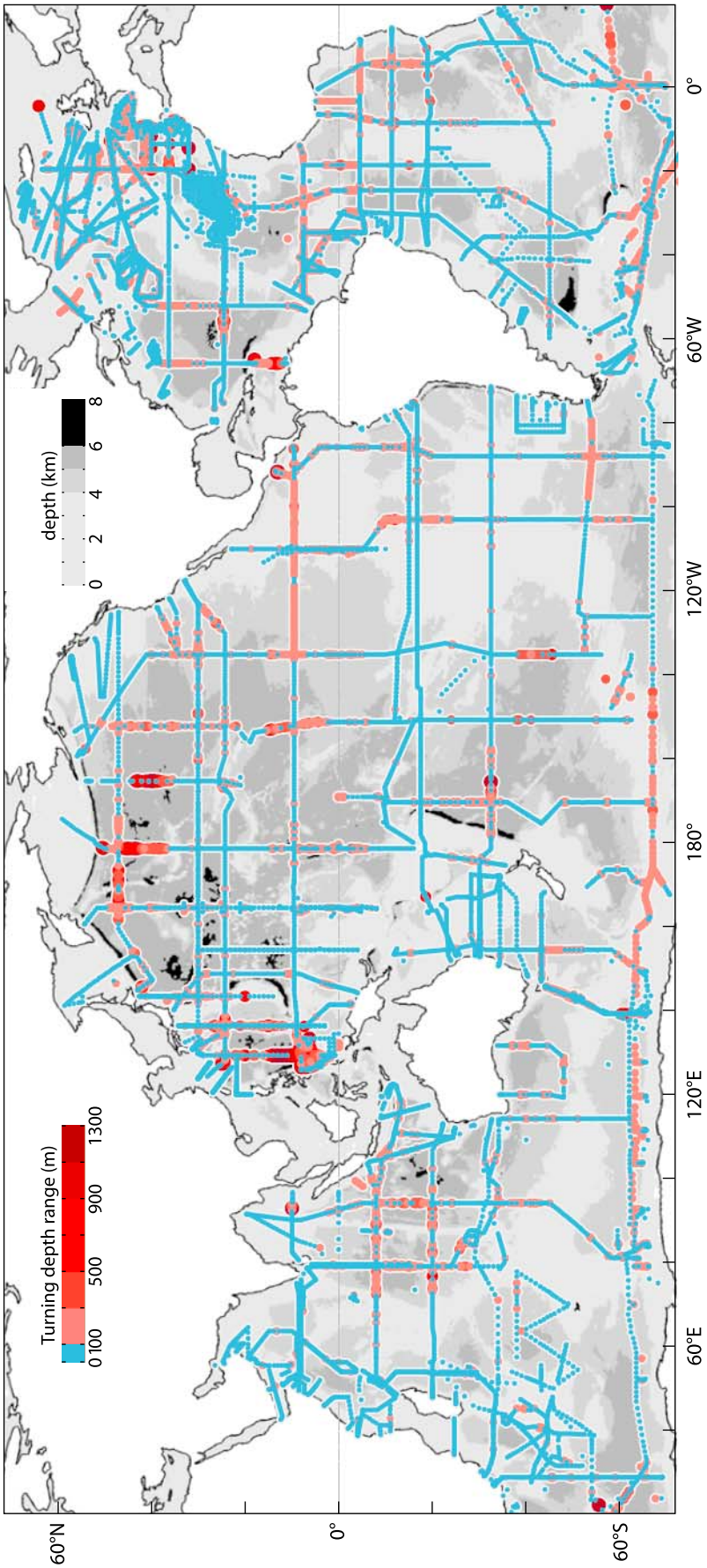

Figure 7. Red dots indicate turning depths of zonally propagating M_2 tides, as deduced from WOCE data. Dark red dots correspond to turning points far above the seafloor, while blue dots indicate casts with no turning depth (cf. color bar). Dots for closely spaced casts are not distinguishable here but are distinguishable on the expanded scale in Figure 8. The gray bar indicates ocean depth.

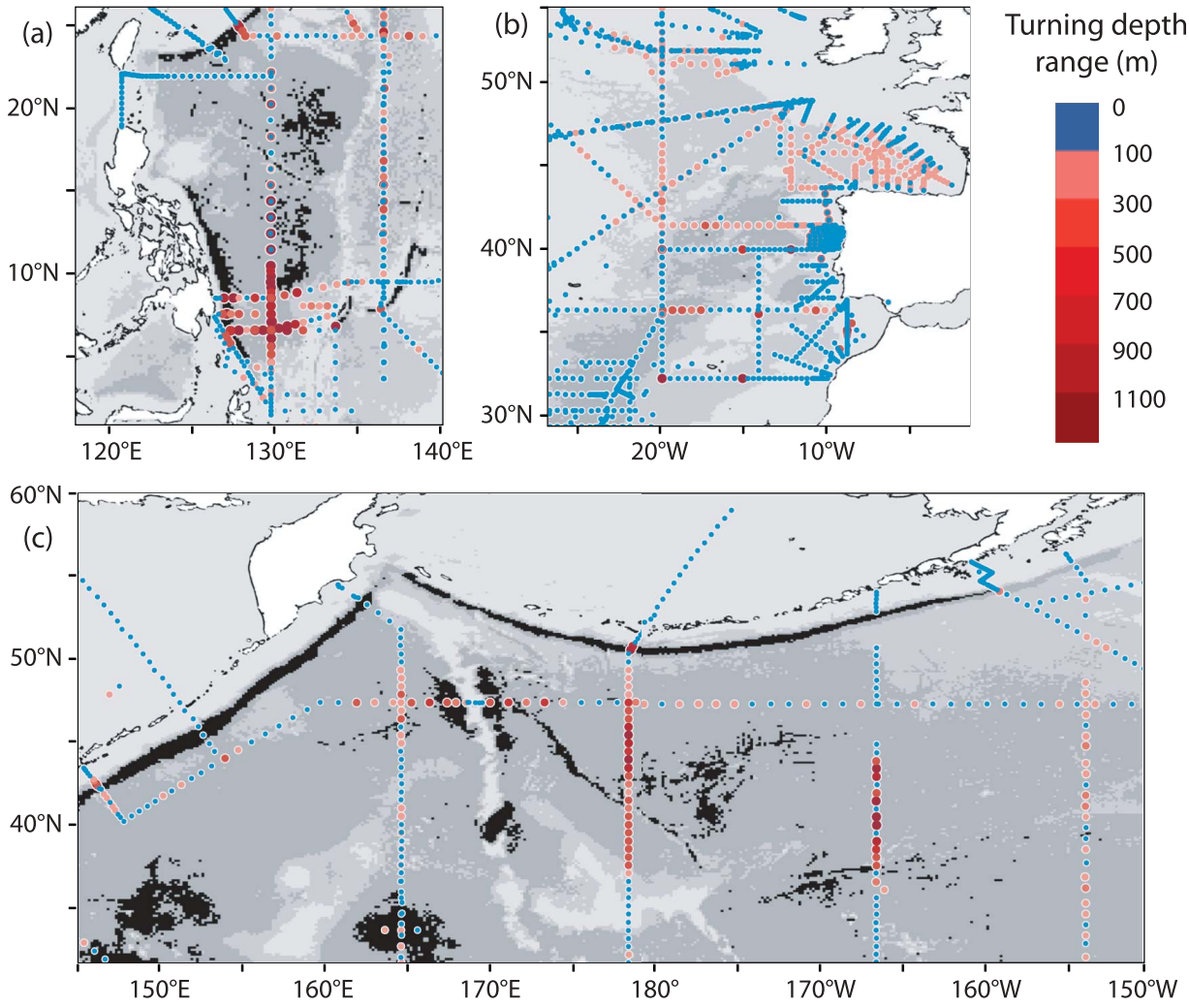

Figure 8. The ubiquity of turning depths in different ocean regions is illustrated by these examples: (a) the Philippine Sea, (b) the Bay of Biscay and further westward in the Atlantic Ocean, and (c) the north Pacific, south of the Aleutian Islands. Dark red dots correspond to turning depths located far above the seafloor, as indicated by the color bar. The background gray scale indicates ocean depth; see gray bar in Figure 7.

Table 2. Incidence of Turning Depths as a Function of Ocean Depth[a]

Depth (km)	Seafloor (%)	Casts
>0	100	18,087
>1	89.3	14,157
>2	84.8	11,956
>3	76.3	9878
>4	54.3	6850
>5	21.6	2212
>6	1.0	54
Depth Range (km)	**Number of Turning Depths**	**With Turning Depths (%)**
0–1	0	0.0
1–2	0	0.0
2–3	0	0.0
3–4	10	0.1
4–5	77	1.1
5–6	229	10.4
>6	21	38.9

[a]Seafloor column gives the percentage of the seafloor below the depth given in the Depth column, Casts column gives the total number of casts in that depth range, Depth Range column gives the depth range, Number of Turning Depths column gives the number of casts in that depth range with robust turning depths (see text), and With Turning Depths column gives the percentage of the casts in that depth range that have turning depths.

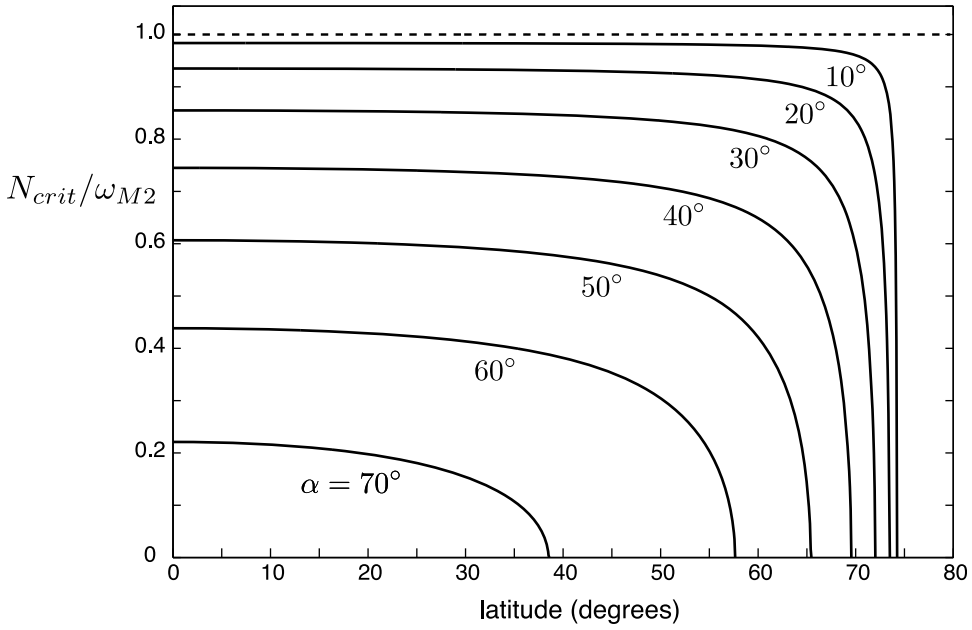

Figure 9. Critical value of N/ω_{M2}, as given by equation (8); for smaller N, the M_2-internal tides cannot propagate. Here the full Coriolis force is taken into account, which introduces a dependence on the angle of propagation α (labeled on the curves) in the horizontal geographical plane, as well as a dependence of N_{crit} on latitude. For zonal propagation ($\alpha = 0$) the result is the same as under the Traditional Approximation (dashed line), but for other directions of propagation the critical value of N is reduced to the point where it disappears altogether when $\alpha > 74.5°$), indicating that internal M_2 tides can propagate in layers of any N.

energy might not contribute to the global internal wavefield as much as would otherwise be expected in the absence of turning depths. Models of the generation of internal tides should include the effect of turning depths, especially if the aim is to study their global role in mixing; to do this correctly, both nonhydrostatic and non-traditional effects need to be taken into account.

Appendix A

[50] We present here the procedures used in our analysis of the WOCE data. These procedures are based on well known statistical methods [e.g., see *Joint Committee for Guides in Meteorology*, 2008; *Lemieux*, 2009].

A1. Effective Degrees of Freedom for Correlated Variables

[51] Suppose one has measurements $T_1, T_2, \ldots T_n$ and that the variables are correlated so that

$$\langle T_i \rangle = \mu; \quad \langle T_i T_j \rangle = \mu^2 + \sigma^2 e^{-\delta|i-j|/\xi}, \tag{A1}$$

where ξ is a correlation length and μ is the mean (this μ is of course unrelated to μ in equation (1)). What is the effective number of degrees of freedom n_{ind} when these measurements are added together? This question can be addressed by asking how well the sample mean $\bar{T}$ estimates the true mean μ. (For simplicity ignore the fact that in practice one does not know μ and has to estimate it.) The expectation value of the square difference between the sample mean and true mean is

$$\left\langle \left(\sum_{i=1}^{n} \frac{T_i}{n} - \mu \right)^2 \right\rangle = \frac{1}{n^2} \sum_{ij} \langle (T_i - \mu)(T_j - \mu) \rangle \tag{A2}$$

$$= \frac{1}{n^2} \left(\sum_{ij} \langle T_i T_j \rangle - \mu^2 \right) = \frac{1}{n^2} \sum_{ij} \sigma^2 e^{-\delta|i-j|/\xi}. \tag{A3}$$

If $n\delta \gg \xi$, it should be legitimate to neglect edge effects. Each value of i contributes an equal term to the sum. The values of j range over those both greater than and less than i. Then one can write the approximation

$$\frac{1}{n} \sum_{j=-\infty}^{\infty} \sigma^2 e^{-\delta|i-j|/\xi} = \frac{1}{n} \sigma^2 \left(1 + 2 \frac{e^{-\delta/\xi}}{1 - e^{-\delta/\xi}} \right)$$
$$= \frac{1}{n} \sigma^2 \frac{1 + e^{-\delta/\xi}}{1 - e^{-\delta/\xi}} = \frac{\sigma^2}{n} \coth(\delta/2\xi). \tag{A4}$$

[53] If the measurements were completely uncorrelated, one would have gotten σ^2/n instead. Thus the effect of correlation can be accounted for by introducing an effective number of degrees of freedom

$$n_{\text{ind}} = n \tanh(\delta/2\xi). \tag{A5}$$

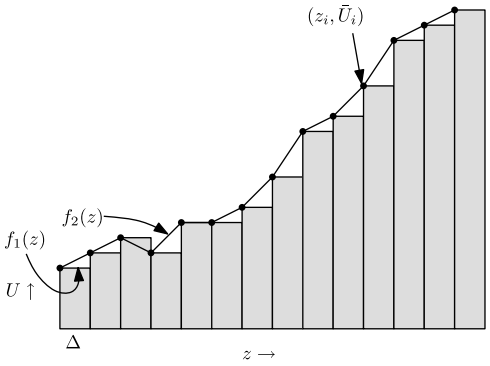

Figure A1. Representation of a set of measurements $U(z)$ by the average values $\bar{U}(z_i)$ in bins of width $\Delta = (z_{i+1} - z_i)$ and by a linear interpretation of the binned values (cf. section A2).

When the correlation length is much greater than the distance δ between successive measurements,

$$n_{\text{ind}} \approx n\delta/2\xi, \tag{A6}$$

which is the result we use in section 3.1.

A2. Optimal Bin Sizes

[54] Suppose one is presented with a set of measurements (z_i, U_i) where the z_i are spaced regularly at intervals δ and the $U_i \equiv U(z_i)$ are noisy measurements of a function $U(z)$. In the case of interest here, U_i corresponds to the results we obtain for the buoyancy frequency squared, $N^2(z_i)$ The noise can be reduced by taking averages of consecutive values of U_i. Create bins of width Δ and average to obtain a new set of measurements $(\bar{z}_j, \bar{U}_j)$, where the averages are taken over the Δ/δ points in each bin. If the bins are too narrow, the function will be very noisy. If the bins are too wide, the true spatial variation of the function is lost. How can one choose the best bin width Δ? For simplicity, we assume that a single uniform bin size is appropriate to describe the data.

[55] The basic idea is the following (for applications of the basic idea to more complex situations, see, e.g., *Shimazaki and Shinomoto* [2007]). Let us adopt two different ways of moving from data points $(\bar{z}_j, \bar{U}_j)$ to a function. Let the first function $f_1(z)$ emphasize smoothing the data, so it gives a better approximation to the true underlying function when the bins are small and the data very noisy. Let the second function $f_2(z)$ emphasize finding trends in the data, so it gives a better approximation when the bins are large, and the variation of $\bar{U}_i$ between them reflects systematic structures one wishes to capture. Then the optimal bin size is found by minimizing the integrated mean square difference between these two different functions.

[56] For function $f_1(z)$ we choose a piecewise constant function with values U_i at points $\bar{z}_i$. For function $f_2(z)$ we connect adjacent points with linear interpolation (Figure A1). That is, in the interval $[z_i, z_{i+1}]$ the first function is

$$f_1(z) = \bar{U}_i \tag{A7}$$

and the second function is

$$f_2(z) = \bar{U}_i + (z - z_i)(\bar{U}_{i+1} - \bar{U}_i)/\Delta.$$

Thus we have the cost function C (defined so as to remove a factor of 3) used in section 3.2

$$\frac{1}{3}C = \sum_i \int_{z_i}^{z_{i+1}} dz\,(f_1(z) - f_2(z))^2, \tag{A8}$$

$$= \sum_i \int_{z_i}^{z_{i+1}} dz(z - z_i)^2(\bar{U}_{i+1} - \bar{U}_i)^2/\Delta^2, \tag{A9}$$

$$\Rightarrow C = \sum_i (\bar{U}_{i+1} - \bar{U}_i)^2\Delta. \tag{A10}$$

Figure 4 shows that this cost function does indeed have a minimum at an intuitively sensible bin size when applied to the WOCE data.

[57] **Acknowledgments.** We thank Bruce Rodenborn for helpful discussions and assistance. The research at the University of Texas at Austin was supported by the Office of Naval Research MURI grant N000141110701 and National Science Foundation grant CBET-0755114. RBS acknowledges support of NSF grant OCE-085147 to the University of Texas at Austin.

References

Apel, J. R. (1987), *Principles of Ocean Physics*, Academic Press, London.
Cushman-Roisin, B. (1996), Lower and upper bounds on internal-wave frequencies in stratified rotating fluids, *Phys. Rev. Lett.*, *77*, 4903–4905.
Eriksen, C. C. (1982), Observations of internal wave reflection off sloping bottoms, *J. Geophys. Res.*, *87*(C1), 525–538.
Feistel, R., and E. Hagen (1995), On the Gibbs thermodynamic potential of seawater, *Prog. Oceanogr.*, *36*, 249–327.
Feistel, R., D. G. Wright, K. Miyagawa, A. H. Harvey, J. Hruby, D. R. Jackett, T. J. McDougall, and W. W. Wagner (2008), Mutually consistent thermodynamic potentials for fluid water, ice and seawater: A new standard for oceanography, *Ocean Sci.*, *4*, 275–291.
Garrett, C., and L. St. Laurent (2002), Aspects of deep ocean mixing, *J. Oceanogr.*, *58*, 11–24.
Gemmrich, J. R., and H. van Haren (2001), Thermal fronts generated by internal waves propagating obliquely along the continental slope, *J. Phys. Oceanogr.*, *31*, 649–655.
Gerkema, T., J. T. F. Zimmerman, L. R. M. Maas, and H. van Haren (2008), Geophysical and astrophysical fluid dynamics beyond the traditional approximation, *Rev. Geophys.*, *46*, RG2004, doi:10.1029/2006RG000220.
Gill, A. (1982), *Atmosphere-ocean Dynamics*, Academic Press, New York.
Goff, J. (2010), Global prediction of abyssal hill root-mean-square heights from small scale altimetric gravity variability, *J. Geophys. Res.*, *115*, B12104, doi:10.1029/2010JB007867.
Gregory, K. D., and B. R. Sutherland (2010), Transmission and reflection of internal wave beams, *Phys. Fluids*, *22*, 106601, doi:10.1063/1.3486613.
Intergovernmental Oceanographic Commission (2010), *The International Thermodynamic Equation of Seawater—2010: Calculation and Use of Thermodynamic Properties*, *Man. Guides Ser.*, vol. 56, U.N. Educ., Sci. and Cult. Organ., Paris. [Available at http://unesdoc.unesco.org/images/0018/001881/188170e.pdf.]
Joint Committee for Guides in Meteorology (2008), Evaluation of measurement data—Guide to the expression of uncertainty in measurement, *Rep. JCGM 100:2008*, Bur. Int. des Poids et Mes., Sèvres, France. [Available at http://www.bipm.org/utils/common/documents/jcgm/JCGM_100_2008_E.pdf.]
Joyce, T. (1988), The WOCE hydrographic programme: A status report, *WOCE Newsl.*, *6*, 7–10.
Joyce, T., and C. Corry (1994), Requirements for WOCE hydrographic programme data reporting, revision 2, *WHPO Publ. 90-1*, Woods Hole Oceanogr. Inst., Woods Hole, Mass. [Available at http://cchdo.ucsd.edu/manuals/pdf/90_1/title.pdf.]
Kamenkovich, V. M. (1977), *Fundamentals of Ocean Dynamics*, Elsevier, Amsterdam.

King, B. (2010), Laboratory and numerical studies of internal wave generation and propagation in the ocean, PhD thesis, University of Texas at Austin, Austin.

Kistovich, Y. V., and Y. D. Chashechkin (1988), Linear theory of the propagation of internal wave beams in an arbitrarily stratified liquid, *J. Appl. Mech. Tech. Phys.*, *39*, 729–737.

Kortzinger, A., J. Schimanski, U. Send, and D. Wallace (2004), The ocean takes a deep breath, *Science*, *306*, 1337–1337.

LeBlond, P. H., and L. A. Mysak (1978), *Waves in the Ocean*, Elsevier, Amsterdam.

Lemieux, C. (2009), *Monte Carlo and Quasi-Monte Carlo Sampling*, Springer, New York.

Lynn, R. J., and J. L. Reid (1968), Characteristics and circulation of deep and abyssal waters, *Deep Sea Res. Oceanogr. Abstr.*, *15*, 577–598.

Mathur, M., and T. Peacock (2009), Internal wave beam propagation in non-uniform stratifications, *J. Fluid Mech.*, *639*, 133–152, doi:10.1017/S0022112009991236.

Mathur, M., and T. Peacock (2010), Internal wave interferometry, *Phys. Rev. Lett.*, *104*, 118501, doi:10.1103/PhysRevLett.104.118501.

Munk, W. (1981), Internal waves and small-scale processes, in *Evolution of Physical Oceanography*, edited by B. A. Warren and C. Wunsch, chap. 9, pp. 264–291, MIT Press, Cambridge, Mass.

National Oceanographic Data Center (2005), World Ocean Atlas 2005: Data Sets and Products, http://www.nodc.noaa.gov/OC5/WOA05/pr_woa05.html, Natl. Oceanic and Atmos. Admin., Silver Spring, Md.

National Oceanographic Data Center (2010), World Ocean Circulation Experiment, 1990–2002, http://woce.nodc.noaa.gov/, World Clim. Res. Programme, Southampton, U. K.

Shimazaki, H., and S. Shinomoto (2007), A method for selecting the bin size of a time histogram, *Neural Comput.*, *19*, 1503–1527.

Smith, W. H. F., and D. T. Sandwell (1997), Global sea floor topography from satellite altimetry and ship depth soundings, *Science*, *277*, 1956–1962.

van Aken, H. (2006), *The Oceanic Thermohaline Circulation: An Introduction*, Springer, New York.

van Haren, H., and C. Millot (2006), Determination of buoyancy frequency in weakly stable waters, *J. Geophys. Res.*, *111*, C03014, doi:10.1029/2005JC003065.

World Ocean Circulation Experiment (1994), World Ocean Circulation Experiment Southern Ocean Atlas: Program information, http://woceatlas.tamu.edu/Sites/html/atlas/SOA_WOCE.html, Dep. of Oceanorg., Tex. A&M Univ., College Station.

Wunsch, C., and R. Ferrari (2004), Vertical mixing, energy and the general circulation of the oceans, *Ann. Rev. Fluid Mech.*, *36*, 281–314.

Zhang, H. P., B. King, and H. L. Swinney (2008), Resonant generation of internal waves on a model continental slope, *Phys. Rev. Lett.*, *100*, 244504, doi:10.1103/PhysRevLett.100.244504.

T. Gerkema, Royal Netherlands Institute for Sea Research, PO Box 59, Texel NL-1790 AB, Netherlands.

B. King, M. Marder, M. Stone, and H. L. Swinney, Center for Nonlinear Dynamics, University of Texas at Austin, Austin, TX 78712, USA. (swinney@chaos.utexas.edu)

R. B. Scott, Institute for Geophysics, University of Texas at Austin, Austin, TX 78758, USA.

H. P. Zhang, Institute of Natural Sciences, Shanghai Jiao Tong University, Shanghai 200240, China.